Supplementary Material

In situ decoration of laser-scribed graphene with TiO_2 nanoparticles for scalable high-performance micro-supercapacitors

Laura Fornasini[a], Silvio Scaravonati[a], Giacomo Magnani[a], Alberto Morenghi[a], Michele Sidoli[a], Danilo Bersani[b], Giovanni Bertoni[c,d], Lucrezia Aversa[e], Roberto Verucchi[e], Mauro Riccò[a], Pier Paolo Lottici[b], Daniele Pontiroli[a,]*

a- Nanocarbon Laboratory, Department of Mathematical, Physical and Computer Sciences, University of Parma, Parco Area delle Scienze 7/A, 43124, Parma, Italy

b- Department of Mathematical, Physical and Computer Sciences, University of Parma, Parco Area delle Scienze 7/A, 43124 Parma, Italy

c- CNR – Istituto Nanoscienze, Via Campi 213/A, 41125, Modena, Italy

d- IMEM – CNR, Institute of Materials for Electronics and Magnetism, Parco Area delle Scienze 37/A, 43124, Parma, Italy

e- IMEM – CNR Institute of Materials for Electronics and Magnetism, Via alla Cascata 56/C - 38123 Povo – Trento, Italy

[*] Corresponding author. Tel. +39 0521 90 5236. E-mail: daniele.pontiroli@unipr.it (Daniele Pontiroli)

Micro-structure of the laser-scribed material

The micro-structure of LSGO material is shown in Figure S1, as obtained from the LightScribe® writing process. The MSC electrodes (inset in Figure S1) consist of about 20 μm width laser-scribed graphene rows, which overlap and merge forming homogenous planar patterns of about 7 μm thickness [1].

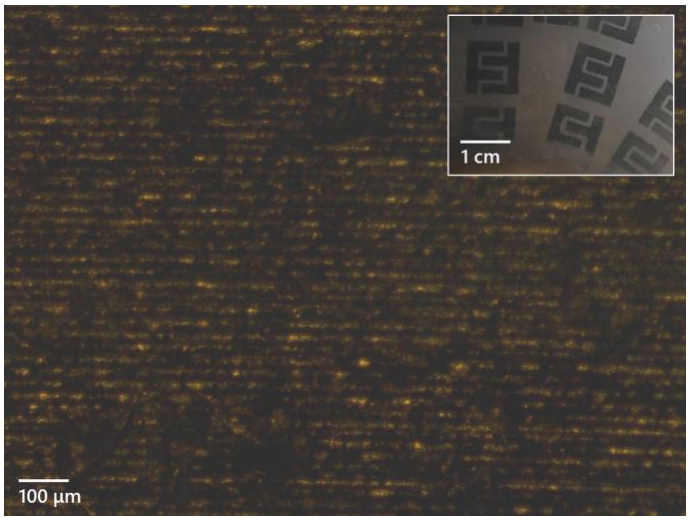

Figure S1. Optical microscope image showing a detail of the micro-structure of the LSGO material. *Inset:* image of the laser-scribed disc section, with electrodes arranged in interdigitated patterns.

Specific surface area of LSGO

The SSA has been estimated using the adsorption of methylene blue by the porous LSGO material [2]. The maximum absorbance peak at 665 nm has been used to evaluate the variation of MB concentration in the solution. A calibration curve of MB aqueous solutions of several known concentrations has been performed to correlate the absorbance and its concentration (Figure S2a), showing that the maximum absorbance is linearly proportional to the MB concentration. The absorbance spectrum of the MB solution after the dye adsorption by the LSGO material is shown in Figure S2b. Since every dye molecule adsorbed

corresponds to a surface area of 1.35 nm^2, the specific surface area of LSGO has been estimated at 180±20 m^2/g.

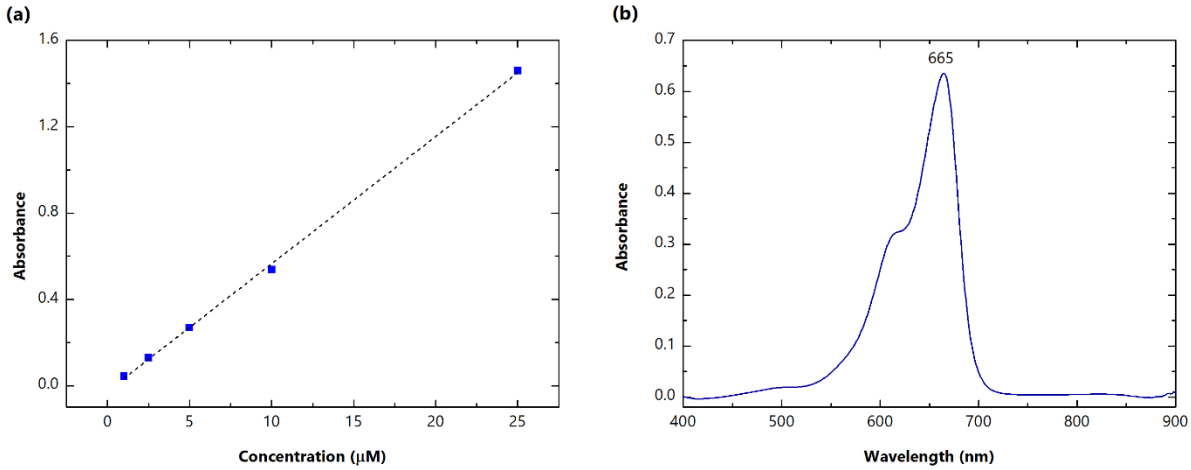

Figure S2. (a) Calibration curve of five MB aqueous solutions of different known concentrations performed to correlate the measured absorbance and the dye concentration (R^2=0.99); **(b)** Typical absorbance spectrum of MB aqueous solution after LSGO adsorption. The maximum absorbance peak at 665 nm is highlighted.

Electrical resistance and conductivity of GO and LSGO

The conversion of GO into LSGO determined an increase in the electrical conductivity of five orders of magnitude, as shown in Table S1. Electrical measurements yield an electrical resistance R=300 Ω for LSGO, corresponding to an electrical conductivity σ~1.1 S/cm. Before the laser treatment, the electrical resistance of pristine GO gives R=27 MΩ, with a σ~$1.6 \cdot 10^{-5}$ S/cm. The increase in electrical conductivity confirms the effect of laser treatment, which induces the conversion from GO, showing insulating behaviour, to LSGO, with much higher electrical conductivity.

Electrode material	Resistance (Ω)	Conductivity (S/cm)
LSGO	300 ± 4	1.1 ± 0.5
GO	$(27 \pm 3) \cdot 10^{6}$	$(1.6 \pm 0.1) \cdot 10^{-5}$

Table S1. Electrical resistance and conductivity of GO and LSGO.

EEL spectroscopy

The EEL spectra from Ti-$L_{2,3}$ and O-K edges are shown in Figure S3. They resemble the spectra from nanostructured anatase [3], in particular regarding the asymmetry of the e_g peak of the Ti-L_3 edge (rutile has the opposite asymmetry of the e_g peak). Quantification of the Ti and O edges gives a Ti/O ratio of 0.46(5) in good agreement with the expected stoichiometry, by considering a small amount of oxygen may derive from the LSGO support film.

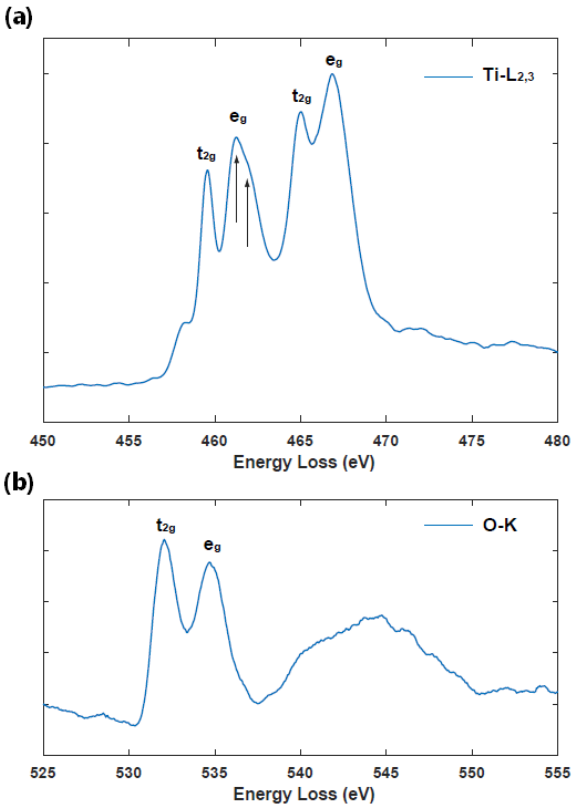

Figure S3. EEL spectra from **(a)** Ti-$L_{2,3}$ and **(b)** O-K edges on TiO_2-LSGO material.

EDS analysis

The elemental composition of TiO_2-LSGO material from EDS analysis is shown in Table S2. The atomic ratio Ti:C is about 1:6, which is in good agreement with the nominal value. Traces of sulfur can be attributed to impurities from the synthesis process of GO, using the Hummers' method [4].

Element	(keV)	Mass (%)	Counts	Error %	Atom %
C K	0.277	42.75	2564.1	0.01	61.00
O K	0.525	25.63	3626.6	0.02	27.45
Ti K	4.508	30.28	5882.5	0.02	10.83
S K	2.307	1.34	302.1	0.33	0.71

Table S2. Elemental composition of TiO_2-LSGO material from EDS results.

Powder X-ray diffraction

PXRD pattern of TiO_2-LSGO material (Figure S4) confirms that anatase is the main TiO_2 crystalline phase in TiO_2-LSGO material, with its most intense (101) reflection at $2\theta = 25.3°$. The nanocrystalline structure of the laser-scribed material is highlighted by the broadening of the (101) diffraction reflection. The mean crystallite size has been evaluated at ~10 nm from the Scherrer equation, showing good agreement with STEM data. A small amount of rutile TiO_2 has also been detected with its (110) and (101) reflections at $2\theta = 27.5°$ and $2\theta = 36.0°$, respectively, as minority phase, estimated as less than 10% of the total TiO_2 mass.

When high-temperature treatments are involved in TiO_2 synthesis, the formation of rutile instead of anatase should be favoured. However, the anatase to rutile phase transition is not instantaneous and several parameters has to be considered (i.e. particle size, particle shape, heating rate etc.). The heat treatment caused by the LightScribe® process is supposed to be shorter than the annealing time required to induce the phase transition. Thus, anatase is the expected main crystalline phase after laser-scribed writing process, as observed from PXRD and from the other analytical techniques (HRTEM, EELS, Raman). Nevertheless, this transition cannot be completely excluded, taking place in small regions of the sample, as confirmed by its minority contribution detected by PXRD analysis.

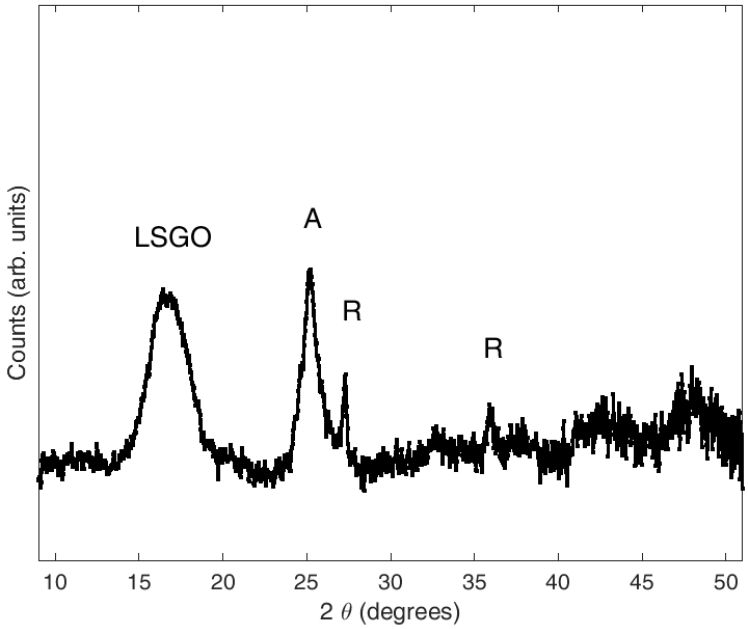

Figure S4. Powder X-ray pattern of TiO_2-LSGO material. The background arising from capillary has been subtracted. Peaks belonging to LSGO, anatase (A) and rutile (R) phases are labeled. The amount of the minority rutile phase has been estimated as less than10% of the total TiO_2 mass.

XPS lineshape analysis on GO and LSGO

C1s and O1s core level lineshapes are analyzed using Voigt functions after the removal of a Shirley background. All peaks have a fixed G-L ratio and symmetric shape, but the graphene main peaks are characterized by a different G-L ratio and an asymmetric lineshape. Uncertainity on peaks' areas is 5%. Results of the lineshape analysis are shown in Table S3.

Core level		GO			LSGO		
		Peak position BE (±0.05 eV)	FWHM (±0.05 eV)	% on tot intensity	Peak position BE (±0.05 eV)	FWHM (±0.05 eV)	% on tot intensity
C1s	C graphene	288.4	1.36	55.9	284.4	1.1	85.6
	C-O	290.8	1.27	28.1	286.8	1.2	2.0
	C=O	292.3	1.63	8.0	288.3	1.6	5.1
	COOR/COOH	294.6	2.00	1.3	290.7	2.03	6.0
	C defects	290.4	1.55	6.7	286.4	1.55	1.3
O1s	O-C	536.7	1.85	73.9	533.3	1.85	38.6
	O=C	535.9	1.7	22.4	532.3	1.73	48.9
	O in COOR/COOH	535.1	1.86	3.7	531.7	2.0	16.5

Table S3. Results of the XPS lineshape analysis on GO and LSGO.

Comparison among different MSCs with laser-scribed graphene-based electrodes

Electrode material	Starting material	Reducing method	C_{sp} (mF/cm^2)	References
Reduced Graphite Oxide (RGO)	GO	CO_2 laser printer	0.5	Gao et al. 2011 [5]
Laser-scribed graphene (LSG)	GO	LightScribe (788 nm laser)	2.3	El-Kady and Kaner 2013 [1]
Laser-induced graphene (LIG)	Polyimide	CO_2 infrared laser	4.0	Lin et al. 2014 [6]
Photochemically Reduced Graphene (PRG)	GO/TiO_2 NPs	UV Hg lamp	1.5	Wang et al. 2017 [7]
LSGO (H_3PO_4/H_2SO_4)	GO	LightScribe (788 nm laser)	4.6/5.6	This work
TiO_2-LSGO (H_3PO_4/H_2SO_4)	GO/TTIP	LightScribe (788 nm laser)	9.9/6.8	This work

Table S4. Comparison among different micro-supercapacitors with laser-scribed graphene-based electrodes.

Electrochemical results of TiO_2-LSGO and LSGO MSCs with PVA/H_3PO_4-based electrolyte

The electrochemical results obtained on LSGO and TiO_2-LSGO electrodes from the CV curves in three-electrode cell configuration are shown in Figures S5 and S6.

In pure LSGO electrode, the CV curves display quasi-rectangular shape in the voltage range 0-1 V vs Ag/AgCl, whereas TiO_2-LSGO electrode shows enlarged CV curves compared to LSGO electrode (Figure S5). Moreover, the three-electrode CV curves of TiO_2-LSGO show the presence of broad peaks, at 0.55 V (Ox) and 0.4 V (Red), respectively, which are clearly not observed in the LSGO CV curves. This behaviour is attributed to the presence of faradic contribution in TiO_2-LSGO electrode, likely due to the TiO_2 nanoparticles.

Furthermore, the mean specific current of CV curves ($<I>_s$) as a function of the CV rate (ν) are plotted in Figure S6, either in the case of LSGO, or in the case of TiO_2-LSGO. In the first case, the trend is linear in the range considered, while in the latter it can be fitted properly by adding a further contribution proportional to $\nu^{1/2}$. Following the known model described by A. J. Bard and L. R. Faulkner [8], this also suggests the presence of faradic contribution in TiO_2-LSGO electrodes.

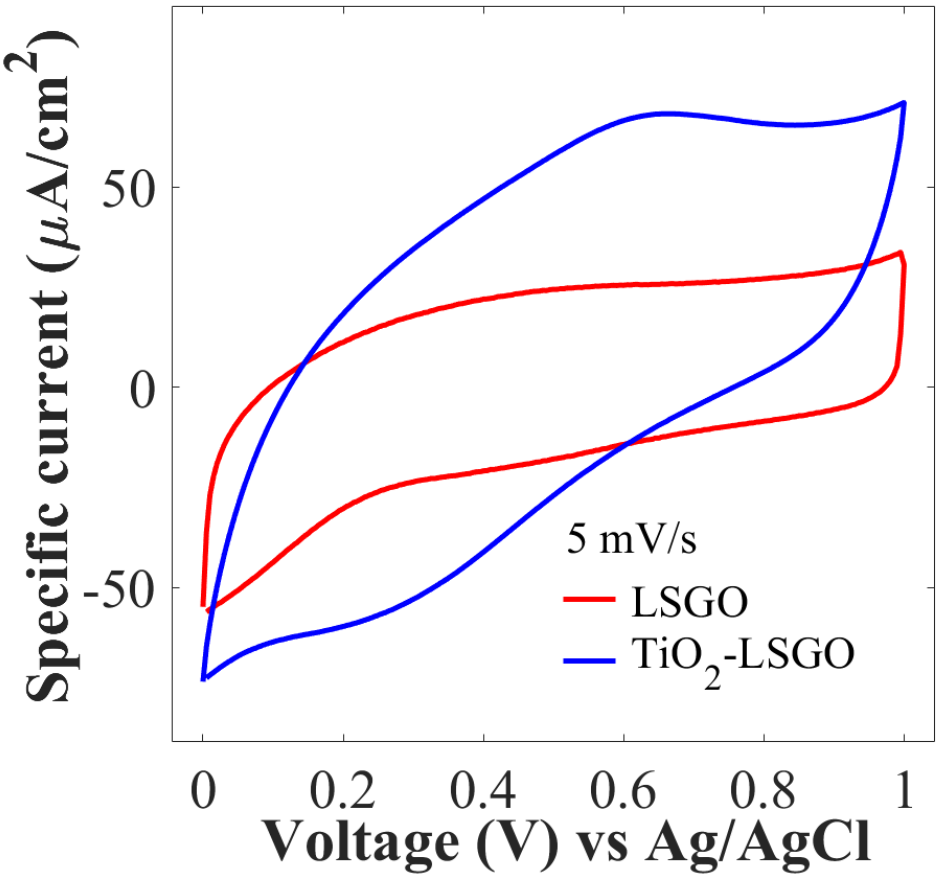

Figure S5. Cyclic voltammetry curves in 3-electrode cell configuration of laser-scribed electrodes with H_3PO_4 aqueous electrolyte at the rate of 5 mV/s.

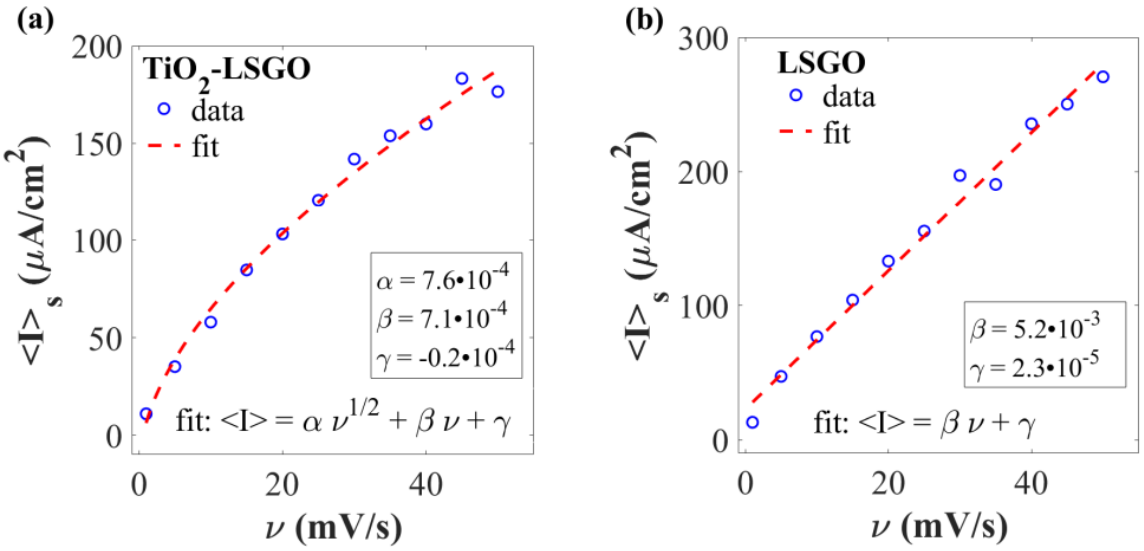

Figure S6. Mean specific current (<I>$_s$) as a function of the CV rate (ν) for **(a)** TiO_2-LSGO and **(b)** LSGO electrodes.

Specific areal energy of MSCs with PVA/H_3PO_4 hydrogel polymer electrolyte is shown in Figure S7, at different current density. At 5 μA/cm^2, TiO_2-LSGO MSCs achieved 0.22 μWh/cm^2, while LSGO MSCs 0.10 μWh/cm^2. The devices reach comparable values of 0.09 μWh/cm^2 at 50 μA/cm^2.

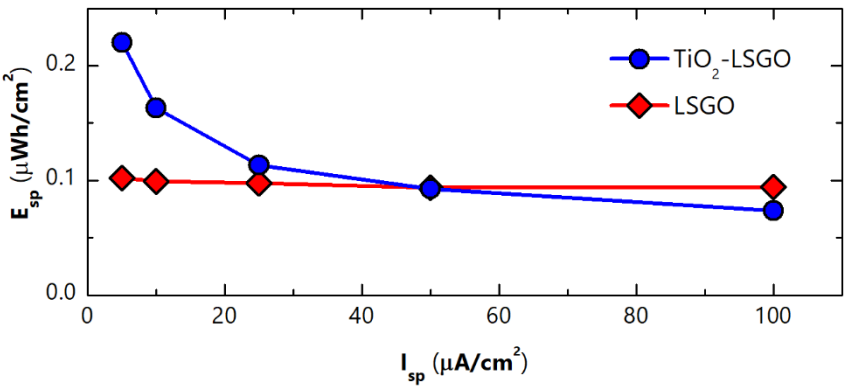

Figure S7. Specific areal energy achieved for TiO_2-LSGO and LSGO MSCs with PVA/H_3PO_4 gel electrolyte at different specific areal currents. Values are averaged on 10 cycles at each specific areal current.

The Coulombic efficiency and the energy efficiency achieved at each cycle for the devices with PVA/H_3PO_4 hydrogel polymer electrolyte are reported in Figure S8. The mean Coulombic efficiency over 3000 cycles is >98% for both MSCs. The energy efficiency after 3000 cycles is about 70%.

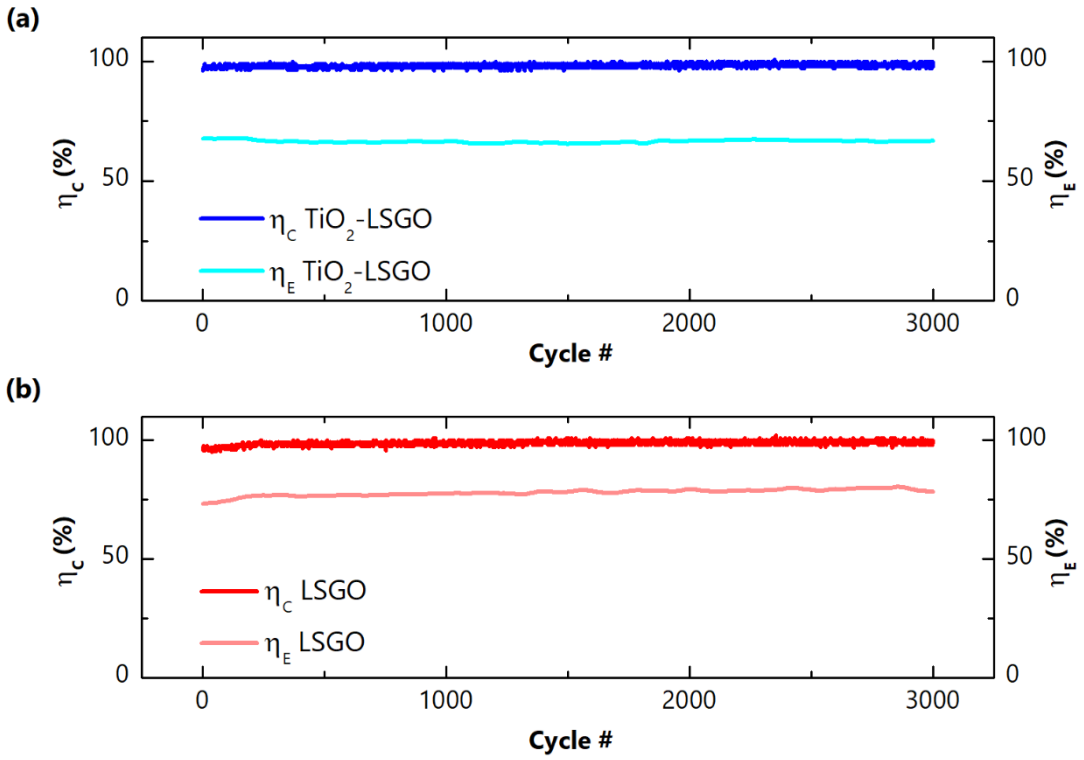

Figure S8. Coulombic efficiency (η_C) and energy efficiency (η_E) for **(a)** TiO_2-LSGO and **(b)** LSGO MSCs with PVA/H_3PO_4 gel electrolyte over 3000 charge and discharge cycles at 5 μA/cm^2.

Electrochemical results of TiO_2-LSGO and LSGO MSCs with PVA/H_2SO_4-based electrolyte

The electrochemical results obtained on LSGO and TiO_2-LSGO electrodes from the CV curves in three-electrode cell configuration are shown in Figures S9. The three-electrode CV curves of TiO_2-LSGO show the presence of broad peaks, confirming that the faradic contribution is ascribed to the presence of TiO_2 nanoparticles (Figure S9).

The results on MSCs with PVA/H_2SO_4 hydrogel polymer electrolyte are shown in Figures S10-S14. As for PVA/H_3PO_4 gel electrolyte, both the capacitive and pseudocapacitive effects are observable in the CV curves of TiO_2-LSGO electrode, in Figure S10a. In contrast, LSGO MSCs show only the EDLC behaviour, with a nearly rectangular CV curve (Figure S10b). Enlargement in the area of CV curves and deviations from the rectangular shape are still observed in TiO_2-LSGO MSCs, confirming the increase in specific areal capacitance. Redox processes, occurring in TiO_2-LSGO MSCs, are highlighted in the comparison at 1 mV/s, in Figure S10c. Faradic effects with slower response time than the EDLC behaviour are confirmed in TiO_2-LSGO devices with PVA/H_2SO_4 hydrogel polymer electrolyte.

GCD curves also proved the twofold behaviour of TiO_2-LSGO MSCs (Figure S11), with deviation from the ideal triangular-shaped curves (concerning purely capacitive electrode materials). As observed for LSGO devices with PVA/H_3PO_4 gel electrolyte, small faradic effects have been induced by the oxygen (still present) content in LSGO material.

Specific areal capacitance, as obtained from the slope of the galvanostatic curves is shown in Figure S12a, at each current density. In TiO_2-LSGO MSCs, the highest specific areal capacitance amounts at 6.8 mF/cm^2 at a current density of 5 μA/cm^2, while the LSGO MSCs gives 5.6 mF/cm^2, at the same current density. At larger current densities, the difference in

specific areal capacitance between the two devices is reduced, up to merge at 50 μA/cm^2, confirming the slower response time of faradic contributions in TiO_2-LSGO. Specific areal energy achieved maximum values of 0.15 μWh/cm^2 in TiO_2-LSGO MSCs, at 5 μA/cm^2 Specific areal energy of MSCs with PVA/H_2SO_4 hydrogel polymer electrolyte is shown in Figure S13, at each current density. At 5 μA/cm^2, TiO_2-LSGO MSC achieved 0.15 μWh/cm^2, while LSGO MSC 0.13 μWh/cm^2. The devices reach comparable values of 0.10 μWh/cm^2 at 50 μA/cm^2. Specific areal energy vs specific areal power is shown in a Ragone plot in Figure S12b. TiO_2-LSGO devices operating with PVA/H_2SO_4 based electrolyte, even though it achieved lower specific areal energy than the corresponding TiO_2-LSGO MSCs with PVA/H_3PO_4 based electrolyte, achieved again a higher specific areal energy compared to LSGO devices, at low rates.

The capacitance retentions over 3000 cycles are compared in Figure S12c. TiO_2-LSGO MSCs exhibits an excellent cycling stability with 89% retention of the initial specific areal capacitance, showing a slightly better overall trend than LSGO MSCs value (80%). Fluctuations observed in the LSGO devices are related to the noise from the low current level, as observed for LSGO MSCs with PVA/H_3PO_4 gel electrolyte. The Coulombic efficiency and the energy efficiency achieved at each cycle for the devices with PVA/H_2SO_4 hydrogel polymer electrolyte are reported in Figure S14. The mean Coulombic efficiency over 3000 cycles gives 99.5% and 92.8% for TiO_2-LSGO and LSGO MSCs, respectively. The energy efficiency after 3000 cycles is about 70%.

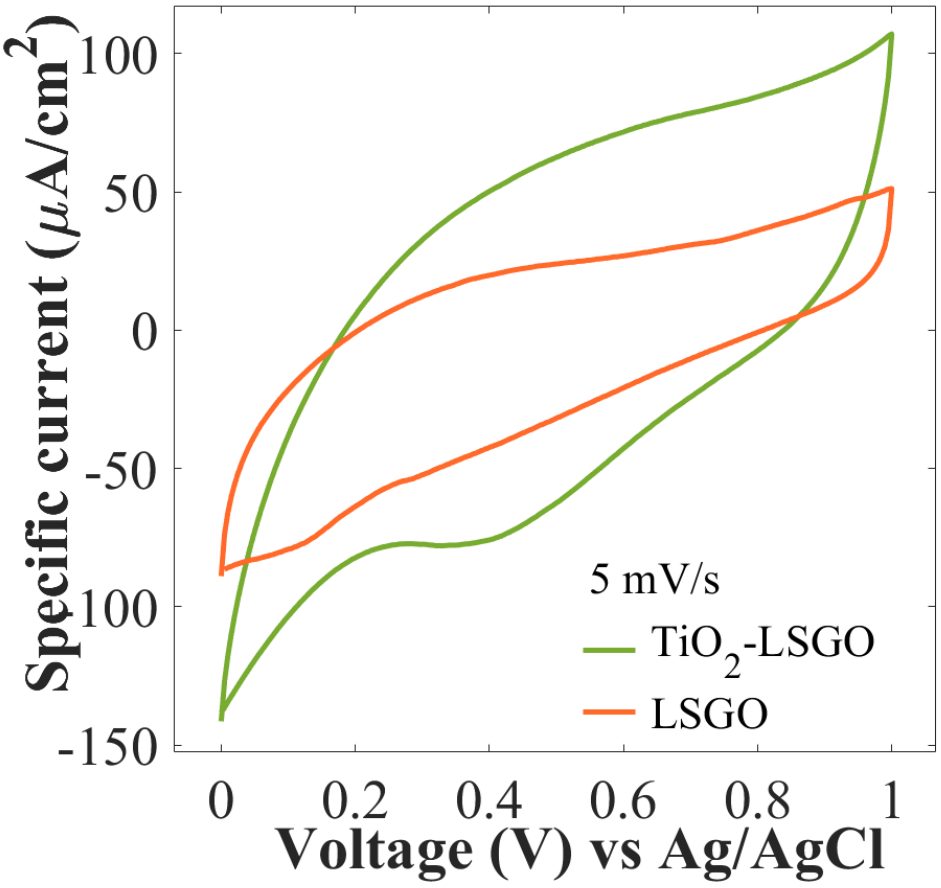

Figure S9. Cyclic voltammetry curves in 3-electrode cell configuration of laser-scribed electrodes with H_2SO_4 aqueous electrolyte at the rate of 5 mV/s.

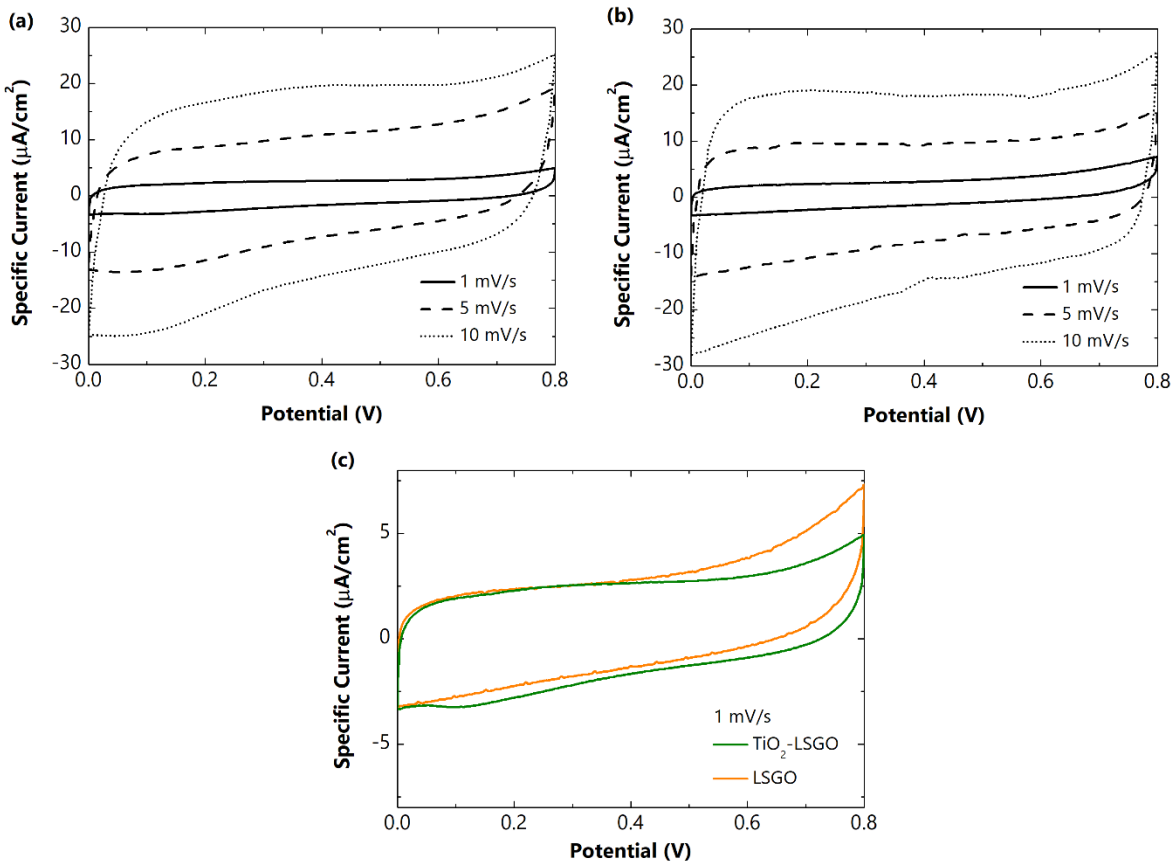

Figure S10. Cyclic voltammetry curves of laser-scribed MSCs with PVA/H_2SO_4 gel electrolyte: **(a)** TiO_2-LSGO and **(b)** LSGO curves at different scan rates; **(c)** TiO_2-LSGO and LSGO curves at the rate of 1 mV/s.

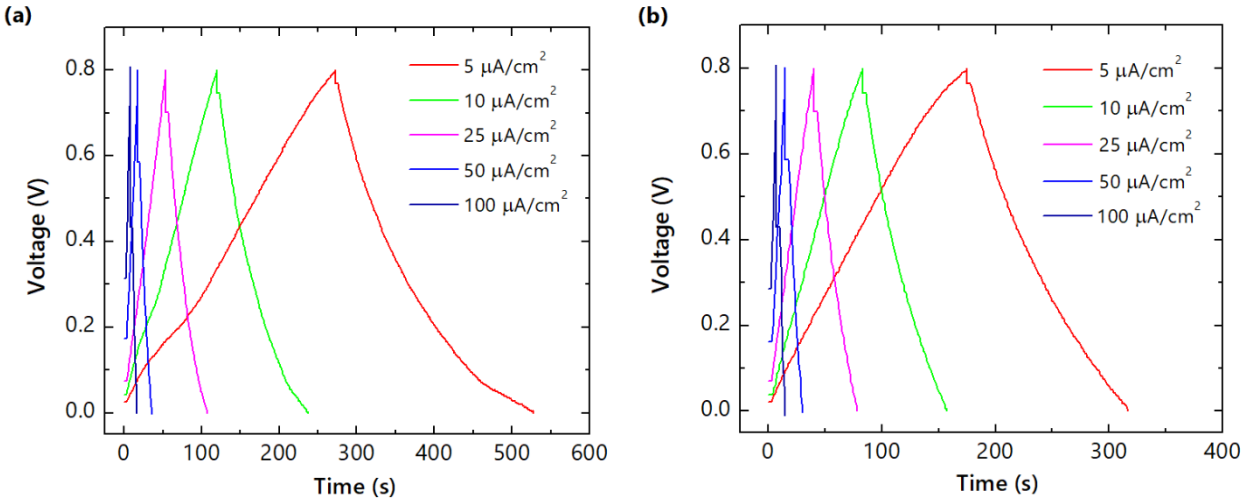

Figure S11. Galvanostatic charge and discharge curves at different specific areal currents of **(a)** TiO_2-LSGO and **(b)** LSGO MSCs with PVA/H_2SO_4 gel electrolyte.

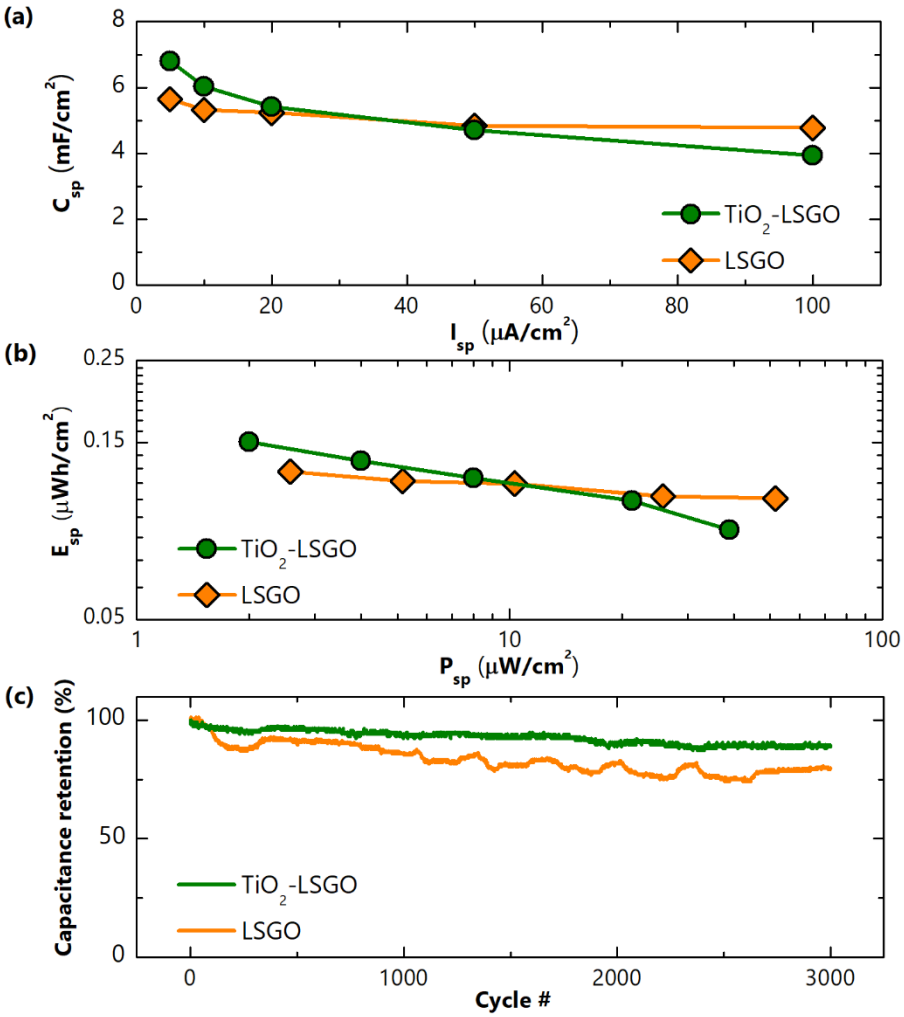

Figure S12. (a) Specific areal capacitance and **(b)** Ragone plot achieved for TiO_2-LSGO and LSGO MSCs with PVA/H_2SO_4 gel electrolyte at different specific areal currents. Values are averaged on 10 cycles at each specific areal current. **(c)** Capacitance retention over 3000 charge and discharge cycles at 5 μA/cm^2.

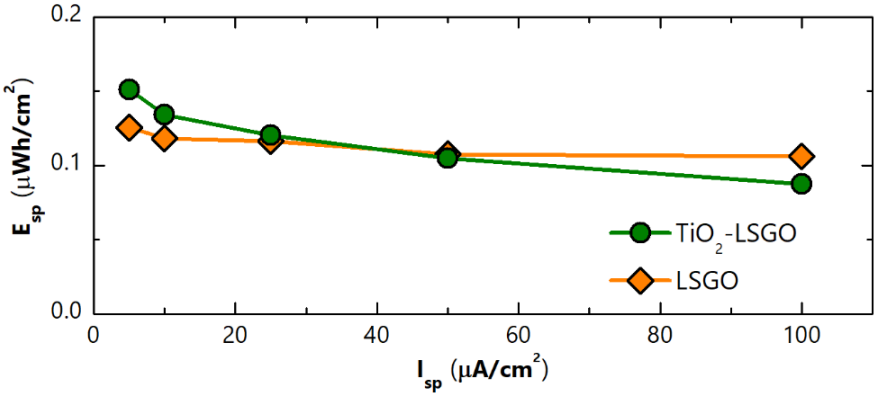

Figure S13. Specific areal energy achieved for TiO_2-LSGO and LSGO MSCs with PVA/H_2SO_4 gel electrolyte at different specific areal currents. Values are averaged on 10 cycles at each specific areal current.

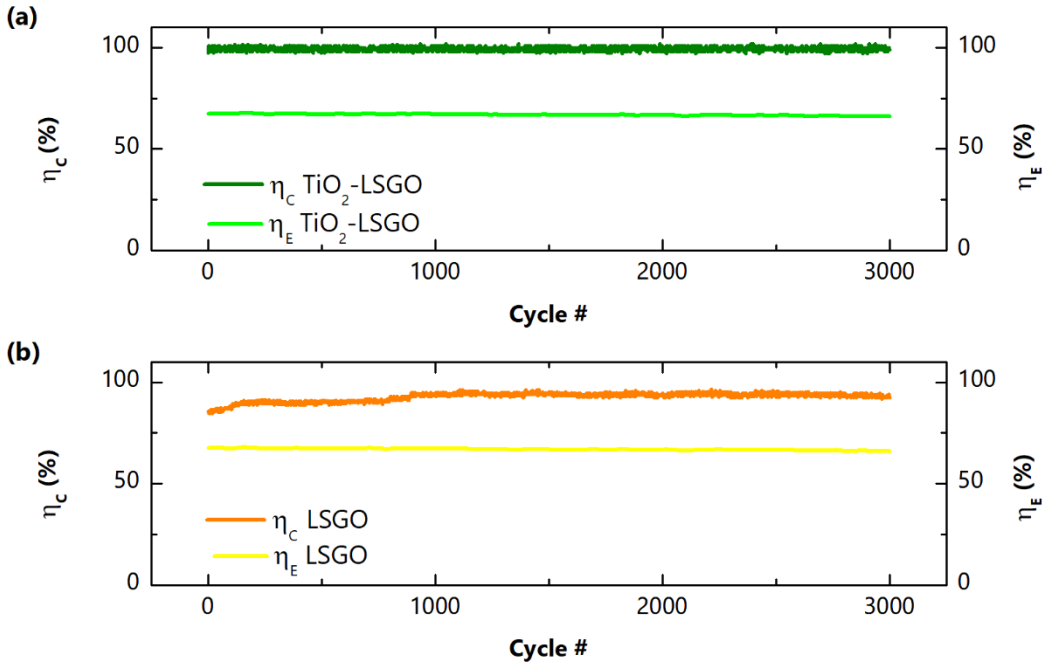

Figure S14. Coulombic efficiency (η_C) and energy efficiency (η_E) for (**a**) TiO_2-LSGO and (**b**) LSGO MSCs with PVA/H_2SO_4 gel electrolyte over 3000 charge and discharge cycles at 5 $\mu A/cm^2$.

Ragone plot comparison among this work MSCs and other graphene-based energy storage devices

In order to compare the electrochemical performance of this work MSCs with other graphene-based devices, the volumetric capacitance (F/cm^3) has also been estimated, considering the thickness of the laser-scribed film. From optical microscope analysis, the thickness of the film is not greater than 10 μm. Thus, the measure of the film evaluated by M.F. El-Kady and R.F. Kaner [1] can be considered as a reference for laser-scribed material obtained by LightScribe® writing process. The volumetric capacitance of MSCs with either PVA/H_3PO_4 and PVA/H_2SO_4 gel electrolytes is shown in Figure S15. Compared to the MSCs obtained by M.F. El-Kady and R.F. Kaner [1], this work MSCs achieved greater volumetric capacitance, amounting at 13.0 and 8.9 F/cm^3 at 13 mA/cm^3 for TiO_2-LSGO devices with PVA/H_3PO_4 and PVA/H_2SO_4 gel electrolytes, respectively.

Ragone plots comparing this work MSCs to different graphene-based energy storage devices, are shown in Figure S16, showing competitive electrochemical performance with the literature data [1,9–11].

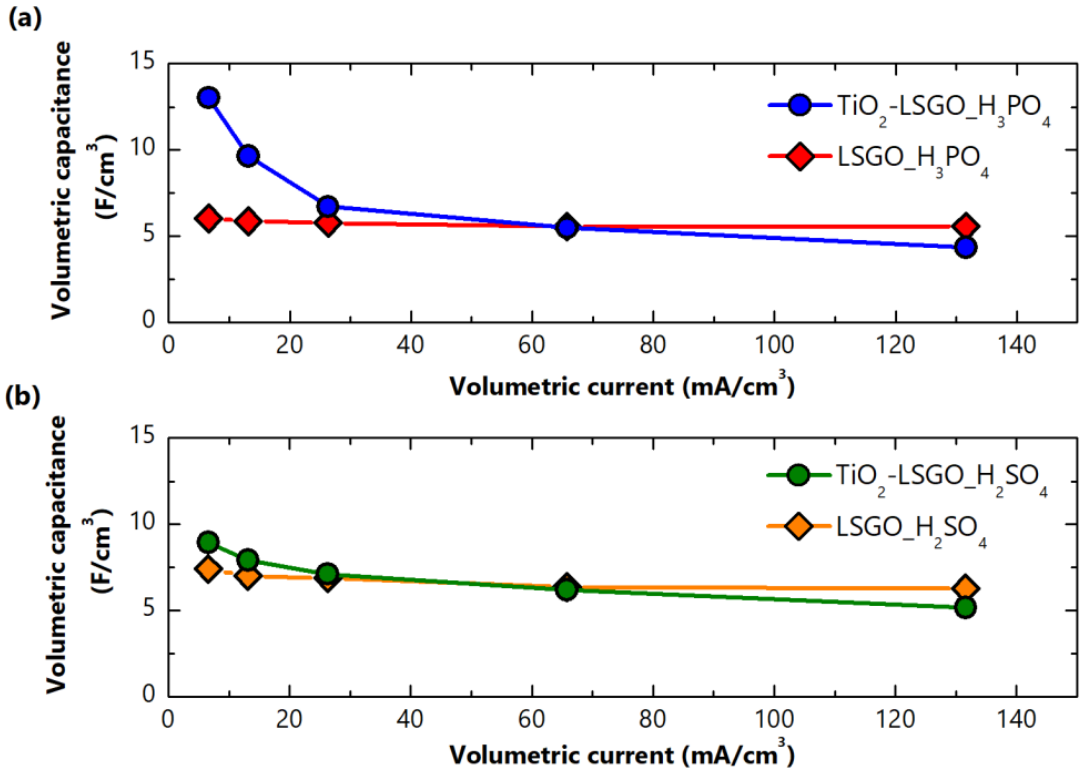

Figure S15. Volumetric capacitance achieved for TiO_2-LSGO and LSGO MSCs with **(a)** PVA/H_3PO_4 and PVA/H_2SO_4 gel electrolytes at different specific areal currents. Values are averaged on 10 cycles at each specific areal current.

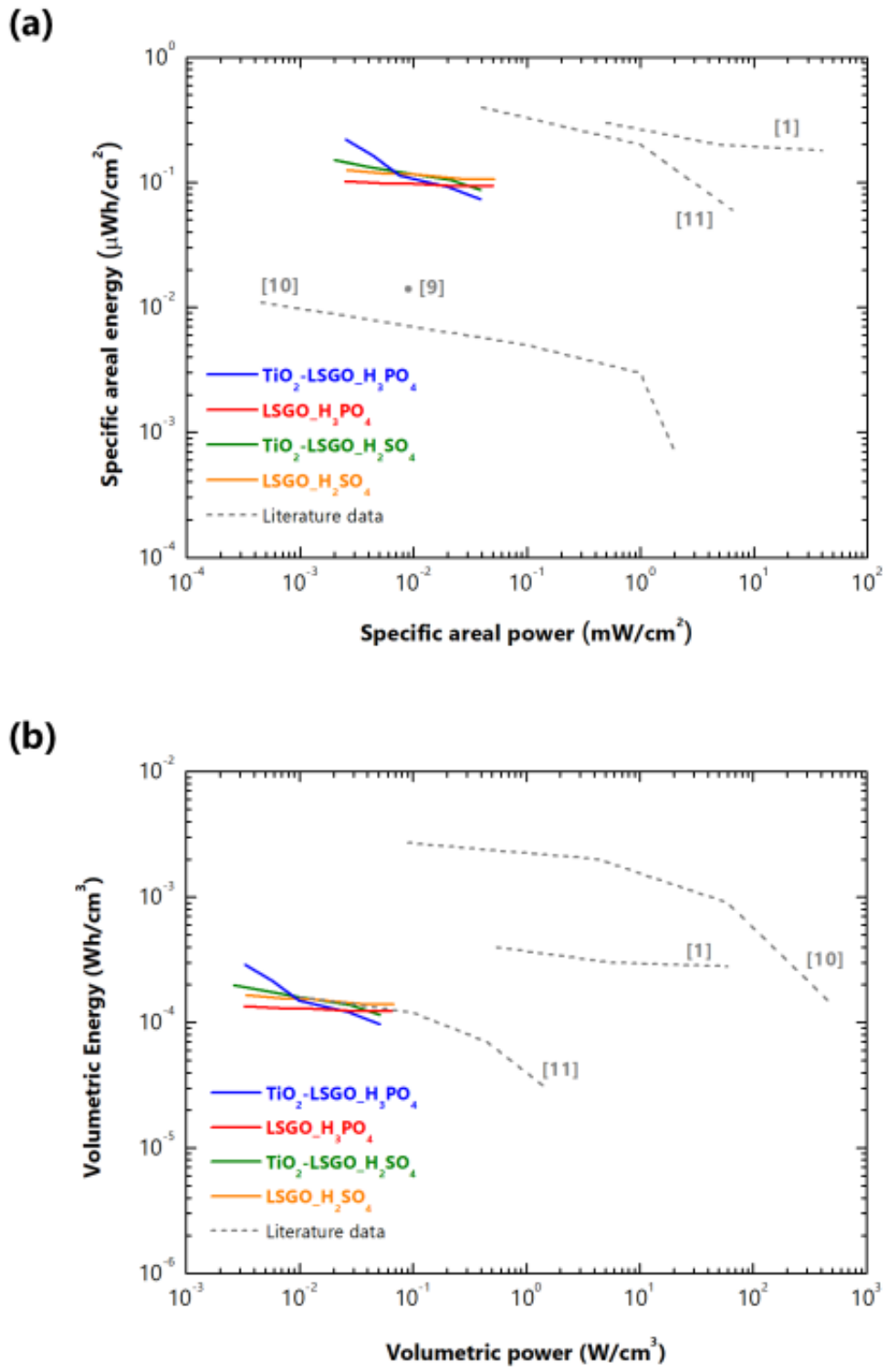

Figure S16. Ragone plot comparison among this work MSCs and other graphene-based energy storage devices: **(a)** specific areal energy as a function of specific areal power; **(b)** volumetric energy as a function of volumetric power.

REFERENCES

[1] M.F. El-Kady, R.B. Kaner, Scalable fabrication of high-power graphene micro-supercapacitors for flexible and on-chip energy storage, Nat. Commun. 4 (2013) 1475–1479. https://doi.org/10.1038/ncomms2446.

[2] M.F. El-Kady, V. Strong, S. Dubin, R.B. Kaner, Laser scribing of high-performance and flexible graphene-based electrochemical capacitors, Science (80-.). 335 (2012) 1326–1330. https://doi.org/10.1126/science.1216744.

[3] G. Bertoni, E. Beyers, J. Verbeeck, M. Mertens, P. Cool, E.F. Vansant, G. Van Tendeloo, Quantification of crystalline and amorphous content in porous TiO2 samples from electron energy loss spectroscopy, Ultramicroscopy. 106 (2006) 630–635. https://doi.org/10.1016/j.ultramic.2006.03.006.

[4] W.S. Hummers, R.E. Offeman, Preparation of Graphitic Oxide, J. Am. Chem. Soc. 80 (1958) 1339. https://doi.org/10.1021/ja01539a017.

[5] W. Gao, N. Singh, L. Song, Z. Liu, A.L.M. Reddy, L. Ci, R. Vajtai, Q. Zhang, B. Wei, P.M. Ajayan, Direct laser writing of micro-supercapacitors on hydrated graphite oxide films, Nat. Nanotechnol. 6 (2011) 496–500. https://doi.org/10.1038/nnano.2011.110.

[6] J. Lin, Z. Peng, Y. Liu, F. Ruiz-Zepeda, R. Ye, E.L.G. Samuel, M.J. Yacaman, B.I. Yakobson, J.M. Tour, Laser-induced porous graphene films from commercial polymers, Nat. Commun. 5 (2014) 1–8. https://doi.org/10.1038/ncomms6714.

[7] S. Wang, Z.S. Wu, S. Zheng, F. Zhou, C. Sun, H.M. Cheng, X. Bao, Scalable Fabrication of Photochemically Reduced Graphene-Based Monolithic Micro-Supercapacitors with Superior Energy and Power Densities, ACS Nano. 11 (2017) 4283–4291. https://doi.org/10.1021/acsnano.7b01390.

[8] A.J. Bard, L.R. Faulkner, Electrochemical Methods Fundamentals and Applications, John Wiley & Sons, New York, USA, 2001.

[9] J.J. Yoo, K. Balakrishnan, J. Huang, V. Meunier, B.G. Sumpter, A. Srivastava, M. Conway, A.L. Mohana Reddy, J. Yu, R. Vajtai, P.M. Ajayan, Ultrathin planar graphene supercapacitors, Nano Lett. 11 (2011) 1423–1427. https://doi.org/10.1021/nl200225j.

[10] Z.S. Wu, K. Parvez, X. Feng, K. Müllen, Graphene-based in-plane micro-supercapacitors with high power and energy densities, Nat. Commun. 4 (2013) 1–8. https://doi.org/10.1038/ncomms3487.

[11] R. Ye, D.K. James, J.M. Tour, Laser-Induced Graphene: From Discovery to Translation, Adv. Mater. 31 (2019) 1–15. https://doi.org/10.1002/adma.201803621.